Applied Thermal Engineering 199 (2021) 117602

Contents lists available at ScienceDirect

Applied Thermal Engineering

journal homepage: www.elsevier.com/locate/ate

Research paper

A predictive model for the industrial air-impingement drying of resin impregnated paper

E. Martín [a,b,*], I. Viéitez [b], F. Varas [c]

[a] Universidade de Vigo. Departamento de Ingeniería Mecánica, Máquinas y Motores Térmicos y Fluidos, Escuela de Ingeniería Industrial, Campus Marcosende, 36310 Vigo, Spain

[b] Instituto Tecnológico de Matemática Industrial (ITMATI), Colegio de San Xerome, Praza Obradoiro, s/n, 15782 Santiago de Compostela, Spain

[c] Universidad Politécnica de Madrid. Departamento de Matemática Aplicada a la Ingeniería Aeroespacial, Escuela Técnica Superior de Ingeniería Aeronáutica y del Espacio, Plaza Cardenal Cisneros, 3, 28040 Madrid, Spain

ARTICLE INFO

Keywords:
Fast predictive model
Heat transfer
Impregnated paper drying
Industrial impingement drying
Optimization models

ABSTRACT

Industrial drying lines of resin-impregnated paper are formed by contiguous furnaces where hot air jets impinge on the surface of the moving paper sheet. The number of production parameters that conditions the process is very high, making the final drying prediction, and the optimal adjustment of the production parameters, very complex tasks. A novel numerical tool for the fast prediction of this industrial drying is presented. The model, obtained from local mass and energy equations for the paper sheet, and fed with results from three-dimensional computational fluid dynamic simulations and thermo-gravimetric tests, determines the evolution of the paper weight along the line for any given combination of production parameters: paper velocity, furnaces air temperatures and mass flows, among others. The model is validated in an industrial line with 11 furnaces, 2 impregnation stages, and more than 150 adjustable operational input parameters, leading to relative errors in the predicted paper temperature evolution and final paper weight of less than 7% and 1%, respectively. Likewise, the model coupling with an optimization tool is also presented to show its capabilities on selecting the best production parameters for prescribed conditions, making the model a useful tool in the framework of the increasingly relevant role of mathematical models in industry.

1. Introduction

This work focuses on the modelling of the continuous drying process of resin impregnated paper carried out by air impinging jets, commonly used in numerous industrial drying operations involving rapid drying of materials in the form of continuous sheets (e.g., tissue paper, photographic film, textiles, and coated paper) [1]. Several phenomena must be accurately modelled, particularly, the description of the liquid transport inside paper sheets, and the estimation of evaporation rates at the paper surface (under particular conditions of the surrounding air). Concerning the first key ingredient, transport in porous media is relevant in a number of technological problems and, as a result, it has been largely considered in the literature (see, for example, [2] or [3] for a review). Although transport in saturated porous media can be easily described by Darcy's law, unsaturated porous media transport (where the porous media is occupied by a mixture of fluids) is much more complex. The effects such as capillarity and mass transfer between phases lead to (strong) non-linear transport properties, depending on saturation and thermodynamical variables [4,5]. The role of pore-scale resolved flows and pore-network structure (to be eventually integrated in continuum homogenized models) is considered, for instance, in [6–11].

Numerical modelling of mass and heat transfer on the surface of porous media has been considered in a large number of studies in the literature (see reviews [12,13]). Available references include idealized and simplified drying configurations such as through air, parallel air flow, normal flow ([14–20]) and turbulent impinging slot jets over flat surfaces ([21–23]). More realistic configurations, such as simplified 2D simulations of impingement jet dryers with multiple nozzles [24] or air flow patterns in a microwave oven [25] are also analysed in the literature.

More relevant to the problem considered here are the works [26] and [27]. The first deals with an experimental study of paper drying using a superheated impinging jet while the second carries out the combined heat and mass transfer modelling of paper drying (considering both impinging air jets and through air drying methods). An analysis

* Corresponding author at: Universidade de Vigo. Departamento de Ingeniería Mecánica, Máquinas y Motores Térmicos y Fluidos, Escuela de Ingeniería Industrial, Campus Marcosende, 36310 Vigo, Spain.
E-mail address: emortega@uvigo.es (E. Martín).

https://doi.org/10.1016/j.applthermaleng.2021.117602
Received 15 June 2021; Received in revised form 30 August 2021; Accepted 15 September 2021
Available online 25 September 2021

Nomenclature

a	Paper sheet width [m]
A_{nozzle}	Nozzle section (straight part) [m^2]
c_ϕ	Parameter (positive) to be adjusted for each specific combination of paper and resin
Co	Concentration of liquid water in the impregnation fluid [%]
$C_p(x)$	Specific heat of the paper [J/(kg K)]
C	Specific heat [J/(kg K)]
d_{nozzle}	Nozzle hydraulic diameter (straight part) [m]
$e_l(x)$	Equivalent thickness of the liquid water in the paper sheet
e_o	Equivalent thickness of the solid part of the paper sheet
e_w	Thickness of the non-impregnated paper sheet
$G(x)$	Paper grammage [kg/m^2]
$h(x)$	Heat transfer coefficient on the paper surface [W/(mK)]
$h_m(x)$	Mass transfer coefficient on the paper surface [m/s]
HE	Specific humidity [kg water vapour/kg air]
HR	Relative humidity [%]
$L_v(x)$	Water latent heat of evaporation [J/kg]
$\dot{m}$	Air mass flow [kg/s]
P	Porosity of the paper
$p_{v,sat}$	Vapour saturation pressure [Pa]
p_{atm}	Ambient pressure [Pa]
Pr_{air}	Air Prandtl number
R	Hydraulic resistance [kg^{-1} m^{-1}]
Re_{ij}	Reynolds number inside each nozzle (straight part)
Sc	Schmidt number
$T(x)$	Paper temperature [K]
T_∞	Air temperature [K]
U_{ij}	Averaged flow velocity inside each nozzle [m/s]
U_p	Paper moving velocity in x direction [m/s]
x	Horizontal coordinate parallel to the moving direction of the paper

Greek symbols

ν_{air}	Air kinematic viscosity [m^2/s]
$\phi(x)$	Drying parameter function
ρ	density [kg/m^3]

Subscripts

b	Bottom paper surface
i	Furnace number
j	Nozzle number (top: $j = 1-5$, bottom: $j = 6-10$)
l	Liquid water
r	Solid part of the resin
t	Top paper surface
v	Water vapour
w	Non impregnated paper
∞	Moist air

Acronyms

CFD	Computational Fluid Dynamics
HTC	Heat Transfer Coefficient

of impingement air drying in papermaking hybrid dryer sections is also studied in [28]. Some other references in the literature deal specifically with different drying techniques quite common in the papermaking industry (see review [29]), such as through air drying [30] or drying in multi-cylinders [31], which are quite different from the drying configurations analysed in this paper.

Unfortunately, literature dealing with resin impregnated paper drying is quite scarce, although presence of resin in the paper can have a strong effect on drying process. In [32] drying and curing of melamine impregnated paper is investigated, focusing on chemical aspects and providing some estimates on curing and evaporating kinetics. Some recent references, such as [33], deal with experimental techniques to on-line monitoring resin and volatile contents.

Concerning the modelling of a whole industrial paper drying line, a number of references can be found (most dealing with papermaking industry units). Usually, coarse models (based on global balances) are used, for instance [34] or [35], which can be easily integrated in a control strategy [36] or used to provide general guidelines concerning operation parameters selection to improve energy efficiency [37–39]. Nevertheless, the paper drying rate of the industrial process analysed in this work is strongly dependent on many local operational details and the use of too coarse/simplified models hinders the derivation of practical detailed guidelines from them.

We present a model whose novelty is threefold: *(a)* it tackles the drying of continuous resin impregnated paper sheet, which is not a well studied problem in the literature, *(b)* it solves the drying problem for realistic industrial operation conditions (far from the idealized conditions assumed in the majority of literature references) and *(c)*, it presents a methodology to build a model capable of retaining all local details of the industrial process, and to integrate them in a very fast numerical tool, which enables the model to be used in multiple tasks, as the optimization of the process or its integration in the process control. The model, whose main outcome is the evolution of the paper weight along the line, is deduced from physical principles of mass and energy conservation and it can be easily adjusted for different lines. Likewise, the coupling of the model to an optimization tool is also presented to show its capabilities on selecting the best production parameters for a prescribed drying degree and/or energy consumption.

The work presented here is organized as follows. The description of the studied industrial drying line is done in Section 2 while the numerical model used to predict the weight evolution of the continuous paper sheet under different production conditions is described in Section 3. Next, the validation of the drying model for the industrial line is carried out in Section 4 while the use of an optimization tool coupled to the predictive model is explained in Section 5. Finally, the main conclusions are summarized in Section 6.

2. Description of the industrial drying line

The analysed industrial drying line is schematically depicted in Fig. 1 (a), where coordinate x indicates the moving direction of the continuous sheet of paper. The line consists of 11 consecutive furnaces, numbered from $i = 1$ up to $i = 11$ (grey domains in Fig. 1 (a)) with two smaller cooling sections (indicated in blue colour), one located after the exit of furnace 4 and the second at the end of the drying line after furnace 11. Each furnace has a total length in the x direction of 3.75 m, being the total length of the line 52.55 m. The roll of paper is threaded at the beginning of production along the whole line, and is then pulled at a constant velocity U_p (in the range of 20 to 40 m/min) and piled up at the end of the line just after the final cooling section. Fig. 1 (b) shows a photograph of the thin sheet of paper entering the first furnace of the line. For convenience, coordinate x is set to 0 at the paper inlet of furnace 1, as indicated in Fig. 1 (a).

At the head of the line, previous to furnace 1, the continuous paper sheet is immersed in a tank with melamine formaldehyde resin diluted in water. The excess of resin is controlled by adjusting the relative position of paper driving rods present ahead of the entrance of furnace 1. Additionally, the paper sheet is showered with the same resin before entering furnace 5. Both impregnation areas are maintained at a small

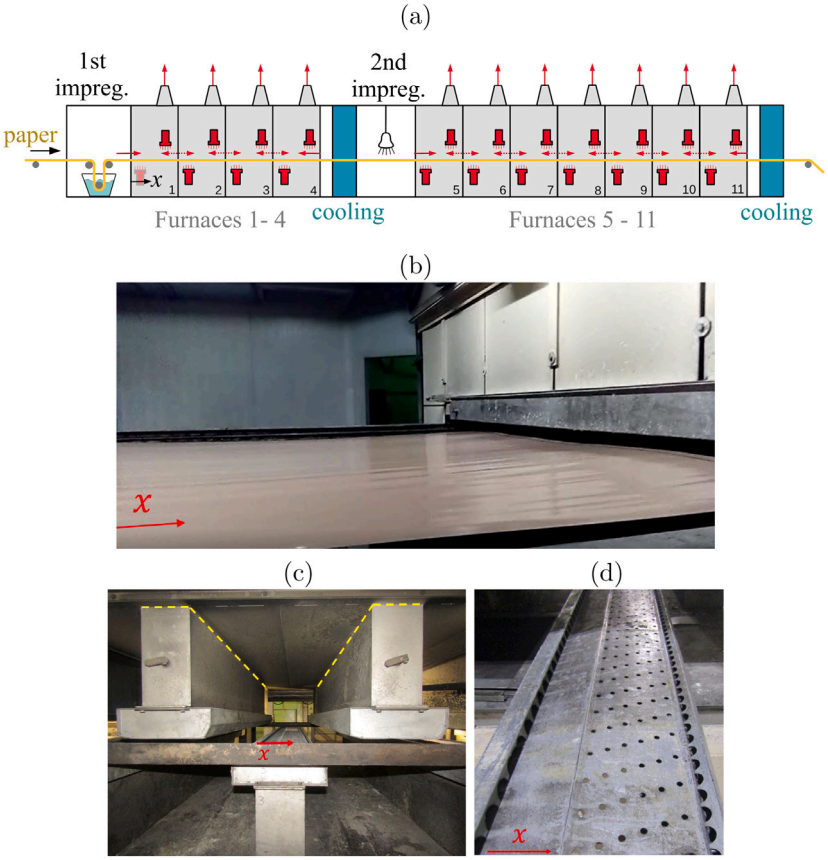

Fig. 1. (a): Schematic configuration of the industrial drying line. Coordinate x indicates the moving direction of the paper.(b): Photograph of the continuous sheet of paper at the entrance of the first furnace. (c): Lateral image of one furnace, where three nozzles are visualized. (d): Geometrical arrangement of the nozzle orifices.

positive gauge pressure to prevent the deposition of particles/debris on the paper. Temperature and humidity inside the impregnation areas are also monitored.

In order to dry the impregnated paper, both sides of the paper sheet are subjected to hot air jet impingement along the 11 furnaces of the line. Each furnace has a total of 10 nozzles that lead hot air to the sheet of paper: 5 located above the paper sheet, named $j = 1$ to $j = 5$ following the moving paper direction x, and 5 below the paper sheet (i.e, $j = 6$ to $j = 10$). Notice that to simplify the sketch of Fig. 1 (a), only two schematic nozzles per furnace are plotted in the sketch, although in the industrial line each furnace has 10 nozzles. Fig. 1 (c) shows the layout of three nozzles inside one furnace. The paper moves in the x direction in the gap between the top and bottom nozzles. When needed, the air mass flow inside each nozzle can be reduced by changing the angle of a gate valve (see the handles in Fig. 1 (c). The heated air impinges both sides of the sheet of paper with a specific pattern given by the geometrical arrangement of the nozzle orifices. Fig. 1 (d) shows the different orifices present at the end of one nozzle through which the heated air exits: two lateral semicircle holes and small circled orifices.

The movement of the heated air inside each furnace is induced by a fan located at its top, as can be seen in Fig. 2 where a sketch of half of a furnace is shown. Each furnace fan can work at different rpms, namely rpm_i, set by the line operator. Before entering the fan, the air is heated at a temperature $T_{\infty i}$ (different for each furnace) by a staggered bank-tube heat exchanger with circulating oil inside. The oil flow inside the heat exchanger is maintained constant, while its temperature can be incremented by the admission (through a controlled valve) of oil at higher temperature. Thus, air heating can be easily controlled, while no direct cooling mechanism is available in the line. To speed the cooling process (for example, when a change of paper type in production requires a lower furnace temperature) there are shutters located on the lateral sides of each furnace that can be opened. Ideally, the shutters should remain closed during production and, in that cases, the furnace chambers do not work at ambient pressure. Once the air passes through the fan, it is driven to the top plenum of the furnace that feeds the 5 top nozzles. The top plenum also feeds the bottom plenum by four lateral ducts, as indicated in the Fig. 2(a). The bottom plenum drives the air to the 5 bottom nozzles to dry that side of the paper sheet. Once the air exits the nozzles , it is discharged inside the furnace chamber and then sucked out through laterals grilles located at the top-lateral sides of the furnace chamber. Finally, part of this recirculated air returns to the heat exchanger and the rest exits the furnace through a chimney located at the top (see Fig. 2). All furnace chimneys are connected to the same extraction line through tubes (of different sizes and lengths). An extractor fan, working at adjustable rpms rpm_e, sucks the air collected from the furnace chimneys to the exterior of the building. Thus, the sucking of the air from each furnace is conditioned by the rpms of the furnace fan and by the sucking pressure at each furnace chimney outlet (that, in turn, depends on the rest of the extraction line). The count of operational parameters is, at least, 23 (11 $T_{\infty i}$, 11 rpm_i and rpm_e).

The furnaces air temperatures $T_{\infty i}$ are monitored continuously, with measurements given by type K thermocouples located at the centre of the bottom plenum of each furnace. For simplicity, the air temperature inside each furnace will be considered uniform in the model and equal to the temperature set point of the heating control system. The specific humidities HE_i are also monitored at specific line locations: inside bottom plenums of furnaces 3 and 4 (named HE_3 and HE_4). The humidity sensors are capable to measure specific humidities in the range from 0 to 1000 g/kg, with a max. process air temperature of 250 °C. Additionally, temperatures and relative humidity in both impregnation chambers are continuously monitored in the line with the same type of sensors. Finally, each furnace of the line has a pyrometer pointing to the

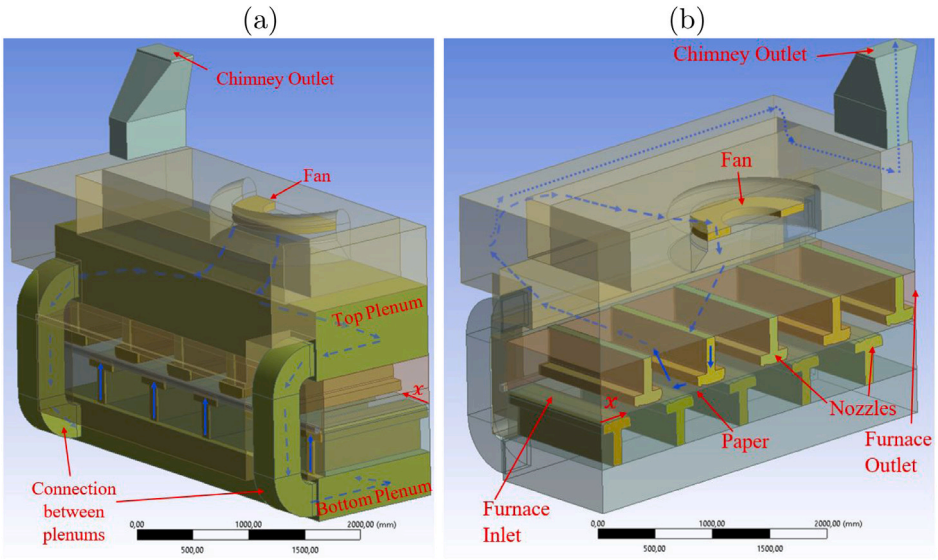

Fig. 2. Schematic configuration of half of a furnace from different perspectives. Coordinate x indicated the paper moving direction. Blue lines show the air flow path. The scale ruler size is 2000 mm.

upper paper sheet surface in order to monitor continuously the paper temperature along the complete line. The pyrometer, which measures temperature up to 250 °C with an accuracy of ±1% of the measuring range, is located at 60 mm of distance from the paper sheet.

3. Numerical model

In order to predict the drying of the paper sheet along the line, it is necessary to know the values of the air mass flows of the 110 nozzles that impinge on both sides of the paper sheet. This quantification is not easy, not only because the geometry of each furnace is complex, but because line neighbour furnaces are coupled between them (air can flow between consecutive furnaces through their respective outlets/inlets) and also with the common extraction line. Horizontal red arrows in Fig. 1 (a) indicate the possible air mass flows directions at the different paper inlets/outlets for each furnace along the drying line. The directions of the air mass flow at the paper inlets of furnace 1 and 5 are known and conditioned by the positive gauge pressure in the impregnation chambers. The directions of the air mass flows at the paper outlets of furnace 4 and 11 are also known. However, direction of air mass flows between consecutive furnaces is not clear and will depend on the production parameters of the line: pressure inside the impregnation chambers, rpms of each furnace fan, air temperature inside each furnace, pressure at each furnace chimney, rpms of the chimneys main extractor fan, gate valve position of each nozzle, etc. Additionally, the global behaviour of the air mass flows inside the line can get even more complicated when specific lateral shutters are partially opened. Therefore, a hydraulic model, capable of quantifying the air mass flows inside the different parts of the line, had to be implemented as a previous step in order to feed the impregnated paper drying model.

3.1. Air mass flow model

Fig. 3(a) shows the hydraulic model used for each of the 11 furnaces of the line. These 11 furnace models are, at the same time, coupled with their respective neighbour furnaces and to the main gases extraction hydraulic model, depicted in Fig. 3(b). F_i stands for the total pressure of the i-furnace chamber, assumed to be homogeneous and constant. Points F_{i-1} and F_{i+1} represent the total pressure of the neighbour (upstream and downstream) furnace chambers. The problem involves the estimation of effective resistances R between different elements of the line.

These resistances (of units $[kg^{-1}m^{-1}]$) account for the total pressure drop between two points (e.g a and b) of the line:

$$\Delta p_{Total\ a\to b} = R\,|\dot{m}|\,\dot{m} \tag{1}$$

where $\dot{m}$ is the air mass flow between point a and b, expressed in [kg/s].

Resistances at the furnace paper inlet and outlet are denoted in Fig. 3(a) by R_e and R_s, respectively, while R_p accounts for the resistance of a (possible) partially open furnace lateral shutter and depends on its opening degree. Resistances R_r, R_c and R_{int} for each furnace stand for the total pressure drop across, respectively: the furnace chamber top-laterals grilles, the path up to the chimney tube, and the tube-bank heat exchanger. On the other hand, R_b represents the resistances across each of the four lateral ducts that lead air to the bottom plenum, while $R_{T_{ij}}(\theta_{ij})$ stands for the resistance across each air nozzle, which depends on the angle of the nozzle valve gate ($\theta_{ij} = 90°$ means the valve is closed).

3.1.1. Resistances estimations using CFD

Resistances were obtained by means of 3D CFD numerical simulations (either of the complete furnace as in Fig. 2, or of specific furnace parts), except for the heat exchangers, grilles and the gases global extraction circuit resistances, which were approximated using hydraulic theory [40,41]. The process followed to obtain the resistances inside a furnace (hydraulic circuit of Fig. 3(a)) was the following:

1. First, simulations of one 3D nozzle configuration (and its valve) impacting on the paper surface were done to calculate numerically the resistances $R_{T_{ij}}(\theta_{ij})$. Steady Reynolds Averaged Navier Stokes (RANS) equations [42] with heat transfer were solved for air with CFD software (based in Finite Volume Methods). Coupled scheme was used to solve the velocity–pressure coupling and second order discretization schemes were selected. Incompressible ideal gas law equation was used for the air density, and buoyancy effects were included in the model. Low-Reynolds $k-\omega\ SST$ was used as turbulent model. Simulations were carried out using an unstructured mesh of approximately 28 millions of cells, in a computational domain as the one shown in the Fig. 4(a), which comprises one nozzle and the paper sheet. At the nozzle inlet, which coincides with the yellow lines of Fig. 1(c), specific air normal velocity value $U_{ij} = 1.5$ m/s

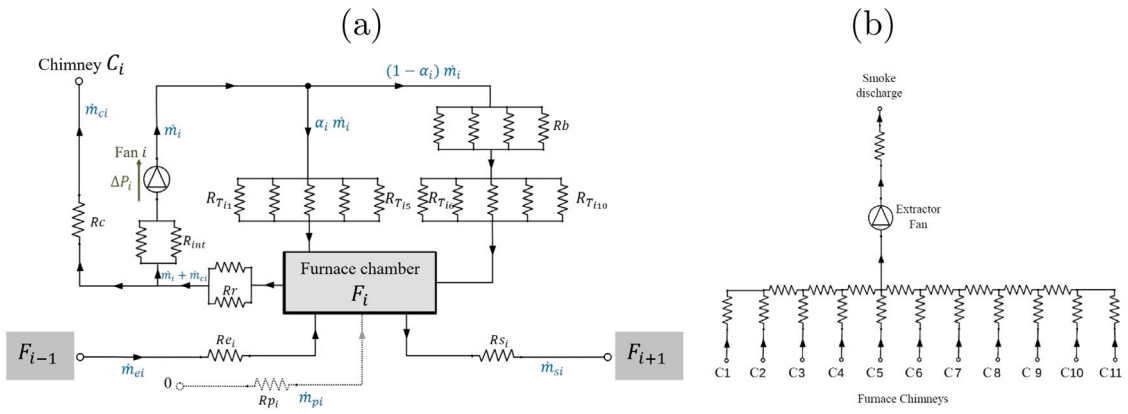

Fig. 3. (a): Hydraulic model for furnace i and (b): for the gases global extraction circuit.

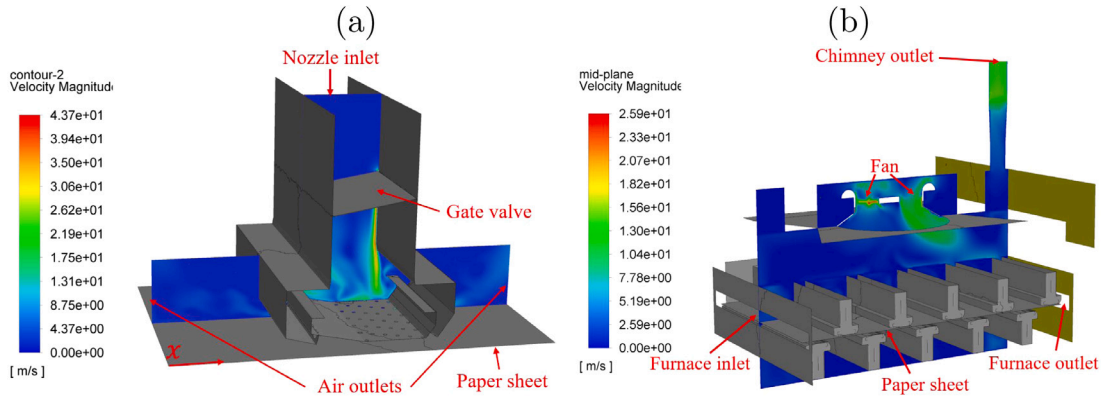

Fig. 4. (a): Velocity field inside a nozzle (for a gate valve angle of 80°) obtained from a 3D CFD simulation of one geometrically detailed nozzle. (b): Velocity field in the middle plane of the furnace for a 3D computational domain of the whole furnace.

and air temperature $T_{\infty i} = 373$ K were imposed. The paper was considered a moving wall of constant x-velocity $U_p = 20$ m/min with a constant temperature $T = 338$ K. No-slip, zero turbulence, and temperature $T_{\infty i} = 373$ K conditions were imposed at the nozzle walls. At the air outlets zero gauge pressure was set while zero-gradient was used for the rest of variables. At the front and back surfaces of the domain, symmetry conditions were selected. The final y^+ value was checked to be lower than 1 in all simulations. A total of 9 different cases (with 9 different valve angles) were simulated to estimate $R_{T_{ij}}(\theta_{ij})$, evaluated from Eq. (1) with the total pressure drop between the nozzle inlet and outlet.

2. Then, simulations of the complete furnace (see half of the domain in Fig. 2) were done with an unstructured mesh of 45 millions of cells. The nozzles exit geometry, as well as the heat exchangers and grilles were simplified to porous regions that create the same pressure losses than the real device (obtained previously numerically, i.e $R_{T_{ij}}$, or using hydraulic theory, i.e R_r, R_{int}). For the heat exchanger porous domain, a uniform volumetric source heat term $q_{he} = 100$ kW/m^3 was included in the energy equation to mimic the air heating system. The furnace fan was modelled in the simulation through an actuator disk (that includes swirl) using the fan performance curve (provided by the fan manufacturer) as input. At the furnace inlet and shutters inlets (when present) a total gauge pressure of 0 was imposed, while at the chimney and furnace outlets zero gauge pressure was set. Velocity wall laws and adiabatic conditions were used as boundary conditions for all walls in the domain. The paper sheet was solved as a moving wall with constant velocity $U_p = 20$ m/min and temperature $T = 338$ K. A total of 25 simulations were carried out for different fan rpms rpm_i and considering different opening degrees of the lateral shutters. One example is shown in Fig. 4(b). For these simulations the final y^+ value was checked to be lower 300. Each simulation took approximately 16 h when solved in 6 cores of 1 Intel-Xeon CPU E5-2620 v3 2.4 GHz processor in a RAM 128 GB workstation. Resistances of paper inlets R_e, paper outlets R_s, shutters R_p (for different open degrees), lateral ducts R_b and furnace internal chimney R_c were obtained from the 3D CFD furnace simulations.

Sensitivity analyses were carried out for all CFD simulations to check grid independence. For the sake of brevity, sensitivity analyses for CFD simulations involved in the drying model are explained later in Section 3.3.

3.1.2. *Implementation and validation of the air mass flow model*

Once the hydraulic resistances are obtained, the hydraulic problem is set and solved. The total pressure jumps across each furnace fan and across the main extractor fan were obtained from the fan performance curves for the given working fan rpms. The discharge of the fumes from the chimneys circuit of Fig. 3(b) is done at ambient pressure. Also, the total pressures at the two impregnation chambers and at the paper outlet of furnace 11 are known and imposed as input conditions in the hydraulic model. Imposing mass flow conservation in the hydraulic circuit junctions and that total pressure losses between two points are independent of the path followed by the fluid, we obtained the complete hydraulic model, which involved the determination of (a minimum of) 57 unknowns and was implemented in free software GNU

Table 1
Production conditions for Test 1.

Test 1											
Paper type	Paper #1										
U_p/U_{nom}[%]	94.4										
Extractor rpm_e/rpm_{nom}[%]	60										
Furnace i	1	2	3	4	5	6	7	8	9	10	11
Fan rpm_i/rpm_{nom}[%]	33	33	33	33	57	57	57	53	53	47	47
$T_{\infty i}/T_{nom}$[%]	67	43	40	41	86	104	100	93	90	80	47
Shutter (left)[%]	0	2.4	55.3	0	0	0	0	1.8	0	22.3	17.6
Shutter (right)[%]	0	0	0.6	0.6	16.5	0	0	0	0	0	0
$HE[g/kg]$	$HE_3 = 15.1,\ HE_4 = 16.4$										
Impregnation conditions	1^{st}: $T = 25°C,\ HR[\%] = 40,\ Co[\%] = 48$ 2^{nd}: $T = 25°C,\ HR[\%] = 40,\ Co[\%] = 48$										

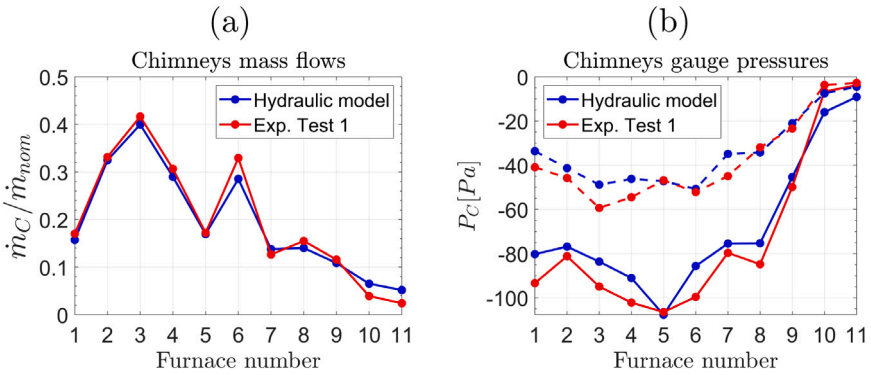

Fig. 5. Chimneys mass flows, (a), and gauge pressures predictions, (b) (solid: static, dashed: total), given by the hydraulic model vs. experimental measurements for Test 1 production conditions.

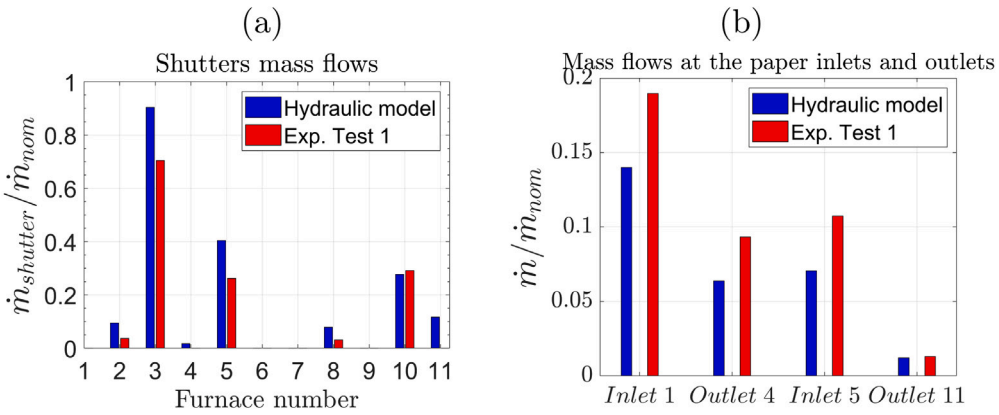

Fig. 6. Mass flows at: (a) the shutters, (b) paper inlets of furnace 1 and 5 and paper outlets of furnaces 4 and 11. Predictions given by the hydraulic model (blue) vs. experimental measurements (red) for test 1 production conditions.

Octave.[1] A total of 159 inputs related to production conditions are needed as inputs in the mass flow model:

- rpms of each furnace fan (11 input values)
- rpms of the main extractor fan (1)
- gauge pressure and temperature at the two impregnation chambers (4)
- air temperature inside each furnace (11)
- opening degree of each nozzle valve (10 × 11)
- opening percentage for each shutter (11 × 2)

The mass flow model provides the total pressures and the air mass flows along the line. The most interesting outputs are the total pressures inside each furnace chamber and the air mass flows inside each of the 110 furnace nozzles, denoted by $\dot{m}_{ij}$. These $\dot{m}_{ij}$ values will be, at the same time, inputs for the paper drying model.

The air mass flow model was validated with experimental measurements and data collected from sensors already installed in the line at six different production conditions. Experimental measurements of velocities, pressures and temperatures were carried out in different accessible locations: the furnaces chimneys, the paper inlet/oulet sections and the shutters. Each furnace chimney has a small orifice that was used to measure velocities, pressures and temperatures. This measurement orifice corresponds to point C_i in the hydraulic diagram of Fig. 3 (a). Velocities, pressures and temperatures were measured at the paper

[1] www.gnu.org/software/octave/

inlets sections of furnaces 1 and 5 and at the paper outlets sections of furnaces 4 and 11. When opened, velocities and temperatures were also measured at the shutters inlet sections.

Velocities were measured with two different devices, depending on the local air flow temperature. For temperatures up to 80 °C, a telescopic hot wire probe KIMO SFC 900 GN of 1 m length coupled to a data-logger module MP210 was used. Precision is ±2% of the measurement for velocities from 0.15 m/s up to 1 m/s, and of a ±3% of the measurement for velocities in the range of 0.15 to 3 m/s. For both velocity ranges the resolution is 0.01 m/s. For velocities from 3.1 to 30 m/s, precision is ±3% of the measurement with resolution of 0.1 m/s. Working temperatures for this probe are restricted from −20 up to 80 °C. As in some regions of the line the working temperatures are much higher (up to 150 °C for some production conditions), a stainless steel pitot tube SR-305 of dimensions 300 × 4 mm was used to measure velocities in these cases. The pitot tube was connected to a differential manometer PCE-PDA 1L, which measures in the range of ±2000 Pa with a resolution of $0.1/1Pa$ and a precision of ±0.5% of the measurement. This manometer was also used for pressure measurements (i.e. in the furnace chimneys).

Comparisons between the numerical results given by the model and the experimental data for six experimental tests, Test 1 up to Test 6, are discussed below. Each test was done in a different day, with the industrial line working at typical production configurations. Table 1 shows the production conditions for Test 1: paper reference (different kinds of paper are processed in this industrial line), paper velocity U_p, rpms rpm_e of the chimneys extractor fan, furnaces fans rpms rpm_i, furnaces temperature $T_{\infty i}$ and opening degree of each furnace shutter. For confidentiality reasons, some operation conditions of the tests (paper velocity, fan rpms, and air furnace temperatures) are indicated in percentage of a constant nominal value U_{nom}, rpm_{nom} and $T_{nom}[°C]$. Paper velocity U_{nom} corresponds to an average of the production velocity values used by the company for different papers. rpm_{nom} corresponds to the nominal rpms of the furnace and gas extraction fans, while $T_{nom}[°C]$ stands for the usual maximum air temperature inside the line. For the sake of brevity, production conditions of Test 2 to Test 6, as well as the opening degree of the 110 nozzle gate valves are included in a supplementary file. Pressure (gauge) values in the two impregnation chambers are the same for all the tests and equal to 0.6 Pa and 0.07 Pa, respectively.

Fig. 5 shows the predicted mass flows and pressures for each of the furnace chimneys for Test 1 conditions and their differences with the experimental data. Again, for confidentiality reasons, all mass flows are re-scaled against the nominal mass flow $\dot{m}_{nom}$, which corresponds to the nominal air mass flow generated by one furnace fan at rpm_{nom} and T_{nom} (with all the nozzle gates completely opened). Numerical results are in good agreement with the experimental ones. Mean relative differences between the predicted and the experimental mass flows values are lower than a 12%, and lower of a 2.5% when considering only furnaces 1 to 10. For the pressure, mean relative differences are of a 6.8% for the total pressure and lower than a 17% for the static pressure (mean relative differences for furnaces 1 to 10 remain below 5.7%).

Fig. 6 shows, respectively, the mass flow predictions for the flow at the shutters and the flow at inlets of furnaces 1 and 5 and outlets of 4 and 5 and their comparison to the experimental values. Though mass flows at shutters are overpredicted and flows at the inlets/outlets are underpredicted, tendencies are well captured by the hydraulic model. Also, experimental measurements in these regions were not as precise as measurements inside the chimneys. The reason is because the sections in shutters, paper inlets and paper outlets are very width (approx. 3 m long) and experimental velocity values show a great deviation depending on the measured point, hindering the estimation of the mass flow for that sections.

Comparison results between predicted and measured values for all tests are summarized in Table 2. Mean relative differences between the predicted and the experimental mass flows values are, in average, of a 9%. For the pressure, mean relative differences are of a 13% for the total gauge pressure and of 12% for the static pressure. Fig. 7 shows the prediction of the flow $\dot{m}_i$ inside each furnace for all the tests, where differences in the mass flows can be observed for different production conditions. This underlines the necessity of having a tool for the prediction of the air flows in the line. Additionally, the air-flow model also provides each of the $11 \times 10 = 110$ nozzle mass flows $\dot{m}_{ij}$ for each combination of the production parameters (not shown here for the sake of brevity). Summarizing, the results show that the mass flow model provides good tendencies for different values of the numerous operation conditions (up to 159) and acceptable results, in the range of what it is expected for a simplified hydraulic model.

Table 2
Averaged relative errors between experimental and predicted values at the chimneys given by the mass flow model for Test 1 to Test 6.

	Test 1	Test 2	Test 3	Test 4	Test 5	Test 6
Mass flow error [%]	12	7.8	8.5	8	8.6	9.8
Static pressure error [%]	17	27	7.5	10	5.5	6.1
Total pressure error [%]	6.8	20	10.2	16	13.4	12.8

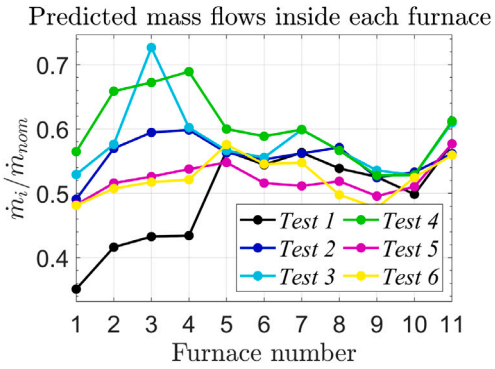

Fig. 7. Predicted mass flows $\dot{m}_i$ in each furnace fan for Test 1 to Test 6 operating conditions.

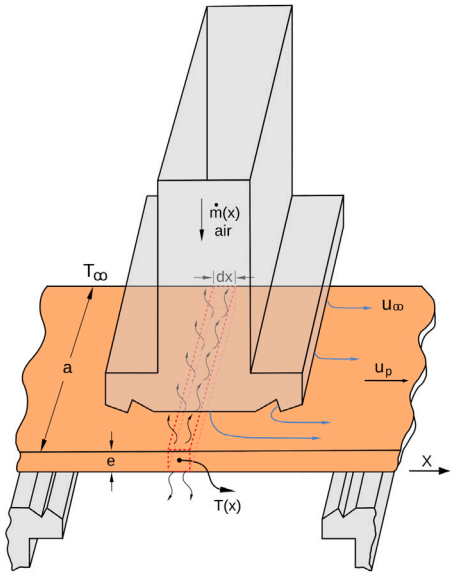

Fig. 8. Sketch of the generic differential control volume (marked in red) located at coordinate x used to apply the conservation equations.

3.2. Drying model

The implemented drying model was derived from applying mass and energy conservation principles to a generic differential control volume,

as the one depicted in Fig. 8, located at a generic coordinate x. The steady control volume, marked in red colour, comprises, at any instant, a portion of the paper sheet of length dx in x direction, width equal to the paper sheet width a, and height equal to the impregnated paper thickness e. As the paper sheet is moving at a constant velocity U_p in the x direction, the impregnated paper enters the lateral left surface of the control volume with a density $\rho_p(x)$ while leaves the lateral right section with density $\rho_p(x+dx)$. At the top and bottom surface of the control volume, the water present in the paper sheet is evaporating. As the front and back surfaces of the control volume are very small (of size $dx \times e$), the possible evaporation in them is considered negligible and it is not included in the conservation balances. For convenience, all the variables and constants involved in the description of the predictive model are expressed in the international system of units.

Grammage $G(x)$ (paper mass per unit area), defined as:

$$G(x) = \rho_p(x) e, \tag{2}$$

is usually the most important outcome of the industrial drying process, therefore, it will be used at the main outcome of the drying model. $G(x)$ along the whole drying line can be decomposed in three parts: G_w, the weight of the paper solid wood/cellulose, G_r, the weight of the solid part of the impregnation solution (that is, the solid resin, which is initially diluted in water), and $G_l(x)$, the liquid water contained in the paper sheet:

$$G(x) = G_w + G_r + G_l(x) \tag{3}$$

As the objective of this process is to retain the resin in the paper, the usual temperatures of the drying line are lower than the evaporation temperature of the solid resin. Thus, the proposed model only takes into account the evaporation of the liquid water contained in the paper sheet. The solid weight G_w before impregnation is known. For example, the validation of this drying model is made for a specific paper (denoted as Paper #1) of $G_w = 70\ gr/m^2$. The solid resin contents G_r can be obtained from the initial paper sheet weight value $G(0)$ just after the impregnation, and from the grade of dilution of the solid resin in the impregnation fluid. For example, if solid resin is diluted in a solution of $Co[\%]$ concentration of water, that means $G_l(0) = Co/100(G(0) - G_w)$ and $G_r = (1 - Co/100)(G(0) - G_w)$.

3.2.1. Mass conservation equation

Considering that the production works under steady conditions (paper velocity U_p, furnace air temperatures $T_{\infty i}$ and nozzles air mass flows $\dot{m}_{ij}$ are constant during production), the following mass conservation equation (4) can be set out, whose terms will be explained next.

$$\frac{dG}{dx} U_p = -\phi(x) \left[h_{m,t}(x)(\rho_v - \rho_{v,\infty})_t + h_{m,b}(x)(\rho_v - \rho_{v,\infty})_b \right] \tag{4}$$

In Eq. (4), the local mass transfer coefficient at the top surface $h_{m,t}(x)$ and the bottom surface $h_{m,b}(x)$ are distinguished. The estimation of these parameters in the model will be explained in Section 3.3.2. Water vapour densities at the paper surface, ρ_v, and in the vicinity air of the paper sheet, $\rho_{v,\infty}$, can be obtained from:

$$\rho_v = \frac{p_{v,sat}(T(x))}{R_v T(x)} \tag{5}$$

$$\rho_{v,\infty} = \frac{p_v(T_{\infty i})}{R_v T_{\infty i}} = \frac{p_{v,sat}(T_{\infty i})}{R_v T_{\infty i}} \frac{HR_i}{100} \tag{6}$$

where R_v is the water vapour constant equal to 461 J/(kg K), $T(x)$ is the paper temperature at that x-coordinate. The vapour saturation pressure $p_{v,sat}$ follows the well known dependency with temperature T:

$$p_{v,sat} = 610.94 \exp\left(\frac{17.625\,(T - 273)}{T - 29.96} \right) \tag{7}$$

while HR_i in Eq. (6) stands for the relative humidity (in %) of the air in the vicinity of paper for each furnace i. As the specific humidity HE_i (mass of water vapour in a unit mass of moist air) is experimentally measured at certain locations of the line, it is more useful to express the dependency of the relative humidity on the specific humidity value:

$$HR[\%] = \left[\frac{HE_i\ p_{atm}}{0.622 + (1 - 0.622) HE_i} \right] \frac{1}{p_{v,sat}} 100 \tag{8}$$

The absolute pressure in Eq. (8) is simplified by the atmospheric pressure.

Parameter $\phi(x)$ in Eq. (4) accounts for several effects. As the paper gets drier, it starts to behave as a non saturated porous media and the water vapour needs to overcome a higher surface tension in order to leave the paper. At the beginning of the line, the parameter ϕ equals 1 as the water in the impregnation fluid is free to be evaporated. As the paper moves forward in the line and gets drier, its value must decrease. Thus, ϕ is related to the liquid water retained inside the paper. Defining $e_l(x)$ as the equivalent thickness of liquid water in the paper, that is, the volume occupied by the liquid water per unit paper area,

$$e_l(x) = \frac{G_l(x)}{\rho_l} \tag{9}$$

and taking into account equation (3), then:

$$\frac{de_l}{dx} = \frac{1}{\rho_l} \frac{dG}{dx} \tag{10}$$

where ρ_l is the density of the water liquid at the paper temperature, assumed to be constant in the model. Thus the evolution of the equivalent liquid thickness follows the paper sheet weight evolution. Based on the models [20] and [27] (used in simpler configurations), we proposed the following modelling for the drying parameter $\phi(x)$:

$$\phi(x) = \frac{1}{1 + c_\phi \left(\frac{e_o P}{e_l(x)} - 1 \right)} \tag{11}$$

where e_o is the equivalent thickness of the solid paper sheet, given by the sum of the non-impregnated thickness e_w plus the equivalent thickness of the solid resin, G_r/ρ_r:

$$e_o = e_w + \frac{G_r}{\rho_r} \tag{12}$$

being ρ_r the density of the solid resin. In Eq. (11), P stands the paper porosity and c_ϕ is an empirical positive constant that has to be adjusted for each paper. Eq. (11) is activated once $e_l(x)$ equals $e_o P$, which represents the void volume present in the non-impregnated paper. Typical values of the non-impregnated paper sheet thickness e_w, and the equivalent thickness of the solid resin $\frac{G_r}{\rho_r}$, are 110 μm and 40 μm, respectively.

Finally, initial conditions for the differential Eq. (4) are provided by the initial paper sheet weight value $G(0)$ at the paper inlet of furnace 1 (after the first impregnation) and, once again, with the value $G(x_5)$, after the second impregnation at the paper inlet of furnace 5.

3.2.2. Energy conservation equation

The conservation of energy applied to the control volume of Fig. 8 can be written in the following form:

$$\begin{aligned} G(x) C_p(x) \frac{dT}{dx} U_p = {} & h_t(x)(T_{\infty,i} - T) + h_b(x)(T_{\infty,i} - T) - \\ & - \phi(x) \left[h_{m,t}(x)(\rho_v - \rho_{v,\infty})_t + h_{m,b}(x)(\rho_v - \rho_{v,\infty})_b \right] * \\ & * \left[L_v(T) + C_v T - C_l T \right] \end{aligned} \tag{13}$$

where the mass conservation equation (4) has been used to simplify the expression. Additionally, the paper conductivity fluxes in the lateral surfaces of the control volume have been neglected, as they are proportional to the paper thickness and, hence, negligible when compared with the rest of the terms of Eq. (13). The same applies for the energy fluxes on the front and back surfaces of the control volume.

The paper specific heat $C_p(x)$ in the previous equation is defined as:

$$C_p(x) = \frac{G_w C_w(x) + G_r C_r + G_l(x) C_l}{G(x)} \tag{14}$$

where C_w, C_r and C_l are the respective specific heat of the non-impregnated paper, the solid resin (1674 J/(kg K)) and the liquid water (4181.3 J/(kg K)). For the non-impregnated paper, the following specific heat dependency on the paper temperature $T(x)$ was taken:

$$C_w[\tfrac{J}{kg\ K}] = 103.1 + 3.87T(x) \tag{15}$$

In Eq. (13), $C_v = 1840\ J/(kgK)$ is the specific heat of the water vapour while L_v stands for the water latent heat of evaporation evaluated at the paper temperature $T(x)$:

$$L_v[\tfrac{J}{kg}] = 2.512 \times 10^6 - 2685.7\ (T(x) - 273) \tag{16}$$

The coefficients $h_t(x)$ and $h_b(x)$ represent the local heat transfer coefficients at the paper top and bottom surfaces, whose values will be deduced in Section 3.3. Integration of differential equation (13) has to be initialized with the paper sheet ambient temperature at the paper inlet of furnace 1, $T(0)$, and once again, after the second impregnation before entering furnace 5, $T(x_5)$. These initial temperatures are considered equal to the temperatures of the two impregnation chambers, which are continuously monitored in the line.

Summarizing, if the mass and heat transfer coefficients $h_m(x)$ and $h(x)$ for the top and bottom paper surfaces are known, Eqs. (4) and (13), with the auxiliary definitions (3), (5)–(6), (9), (11) and (14), provide a model to obtain the coupled evolution of the paper weight $G(x)$ and paper temperature $T(x)$ along the line.

3.3. Derivation of local heat and mass transfer coefficients

Both heat and mass transfer coefficients are obtained using detailed 3D CFD simulations of the transport and heat transfer of the gases (air (O_2, N_2) + water vapour) around the paper sheet. In the case of the mass transfer coefficients, experimental tests at lab scale were also needed. The numerical problem, also solved using software based on Finite Volume Methods, is described by the following steady RANS conservation equations of mass (17)–(18), momentum (19) and energy (20):

$$\nabla \cdot (\rho\, \vec{v}\, Y_k) = \nabla \cdot \left(\rho D_{eff} \nabla Y_k\right) \tag{17}$$

$$\nabla \cdot (\rho\, \vec{v}) = 0 \tag{18}$$

$$\nabla \cdot (\rho\, \vec{v}\vec{v}) = -\nabla p + \rho \vec{g} + \nabla \cdot \left(\mu_{eff}(\nabla \vec{v} + \nabla \vec{v}^T)\right) \tag{19}$$

$$\nabla \cdot (\rho H \vec{v}) = \nabla \cdot \left(k_{eff} \nabla T\right) \tag{20}$$

Y_k stands for the mass fraction of each of the gas species in the gas mixture. Thus, the sum of the three species mass fractions equals 1. ρ is the density of the gas mixture, that follows the incompressible ideal gas law (21), with R_u the universal gas constant and W_k the species molecular weight:

$$\rho = \frac{p_{atm}}{T R_u \sum_{\forall k} \frac{Y_k}{W_k}} \tag{21}$$

Specific enthalpy of the mixture H in Eq. (20) is defined as

$$H = T \sum_{\forall k} C_{p,k} Y_k \tag{22}$$

Effective mass diffusion, effective viscosity and effective thermal conductivity are defined as:

$$D_{eff} = D_m + \frac{\nu_t}{Sc_t},\quad \mu_{eff} = \mu(T) + \rho \nu_t,\quad k_{eff} = k_m + \frac{\nu_t \rho C_p}{Pr_t} \tag{23}$$

where the mass diffusion of water vapour in air was set to D_m = 3.58 10^{-5} m^2/s, viscosity μ is obtained for each temperature using the Sutherland equation, and mixture thermal conductivity k_m is obtained from (24):

$$k_m = \sum_{\forall k} k_k Y_k \tag{24}$$

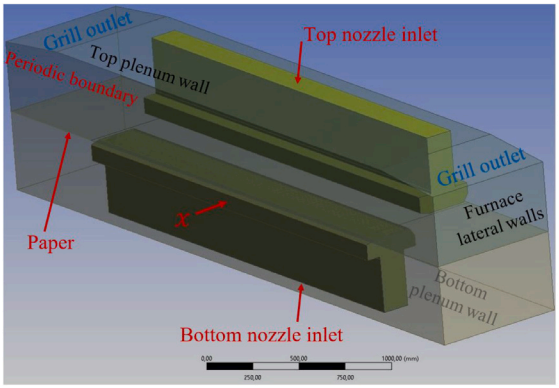

Fig. 9. Computational domain used for the heat and mass transfers coefficients CFD calculation.

The selected turbulent Schmidt number Sc_t and turbulent Prandtl number Pr_t were 0.7 and 0.85, respectively, while the kinematic turbulent viscosity ν_t was obtained from the (low Reynolds) RANS turbulent model $k-\omega$ SST.

The computational domain used in the simulations, shown in Fig. 9, corresponds to part of the furnace chamber. It includes two consecutive nozzles (one over and one below the paper sheet), the paper (top and bottom) surfaces, and the corresponding part of the furnace chamber comprised between the lateral furnaces walls, the top and bottom plenums walls and the grills outlets. Periodic boundary conditions were imposed in the side boundaries that connect with the rest of the non-simulated furnace chamber. The nozzle inlets in the computational domain corresponds to the yellow lines marked in Fig. 1 (c). A uniform temperature $T_{\infty i}$ = 373 K and velocity U_{ij} was imposed in the nozzle inlets. The selected velocity U_{ij} is the averaged velocity inside of the nozzle inlet (see section A_{nozzle}, equal to 0.395 m^2, marked in yellow in Fig. 1 (c)), which can be expressed in terms of the nozzle inlet mass flow $\dot{m}_{ij}$ given by the air mass flow hydraulic model:

$$U_{ij} = \frac{\dot{m}_{ij}}{\rho_{\infty i} A_{nozzle}} \tag{25}$$

Only three simulations, corresponding to three different nozzle inlet air flows values $\dot{m}_{ij}$ ($2\%\dot{m}_{nom}$, $6\%\dot{m}_{nom}$ and $12\%\dot{m}_{nom}$) were used in order to quantify the effect of convection in the heat and mass transfer coefficients. The simulations were carried out considering a constant paper surface temperature of T = 338 K. The paper sheet was considered as a moving wall, of velocity U_{nom}, in the x direction. An injection of a constant vapour flux $\dot{m}_v$, coming from the paper surface, was imposed as boundary condition. This injected vapour mass flow value was taken from averaged values observed along the complete line for the nominal paper velocity, that is, $\dot{m}_v = \frac{G(0) - G(x_{end,11})}{L/U_{nom}}$, where $L = 11 \times 3.75$ m is the length of the drying part of the line. For the rest of the walls, no-slip conditions and zero turbulence values were imposed. For the grill outlets, a zero gauge pressure was selected.

A stationary solver with Coupled pressure-based scheme and second order discretization schemes for mass, momentum, energy and turbulence equations were used. For the case with $\dot{m}_{ij} = 6\%\dot{m}_{nom}$, a sensitivity analysis was carried out using four different unstructured meshes (formed of tetrahedrons and prisms cells). For these four simulations, the global heat flux Q over the paper sheet were computed. The relative variations of Q for each mesh (taking the value given by the finer mesh as reference), ε, were computed and indicated in Table 3. As the relative variation of Q for Mesh#3 and Mesh#4 is of a 1.1%, Mesh#3 was selected as a good compromise between precision and computational effort. For Mesh#3, the $y+$ value was checked to be less than 1 for all the wall boundaries of the domain.

The integration of the numerical results into the drying model is explained next in Sections 3.3.1 and 3.3.2.

Table 3
Sensitivity of paper global heat flux to mesh size.

Mesh	Paper sizing[mm]	$N°Cells$	Q[W]	$\|\epsilon\|$[%]
#1	8	16×10^6	3210	6.4
#2	4	21×10^6	3557	3.7
#3	2	40×10^6	3468	1.1
#4	1.5	64×10^6	3430	ref.

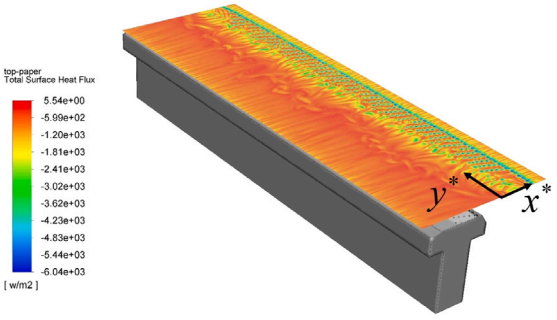

Fig. 10. Local heat flux $q(x^*, y^*)[W/m^2]$ at the top surface of the paper sheet obtained from the 3D CFD simulation for air flows equal to $\dot{m}_{ij} = 6\%\dot{m}_{nom}$.

3.3.1. Heat transfer coefficient profile $h(x)$

Fig. 10 shows the numerical heat flux "footprint" on the surface of the paper sheet just below one nozzle of the computational domain. Horizontal coordinate y^* runs the paper sheet width while x^* is a local nozzle x-coordinate parallel to the paper moving direction.

For each of the three different simulated nozzle mass flow values $\dot{m}_{ij}$, the averaged heat transfer coefficient $\bar{h}$ on each paper side was computed. No significant differences were observed between the top and bottom nozzles in terms of the averaged heat transfer coefficient. The following dependency of $\bar{h}$ with the mean nozzle velocity U_{ij} was found:

$$\bar{h} = 36.9\ 7U_{ij}^{4/5} + 0.4 \tag{26}$$

In order to obtain the heat transfer coefficient dependence on the x coordinate, the local heat transfer coefficient $h(x^*, y^*)$ for each side of the paper was averaged along the paper width direction y^*, and the resulting coefficient was made dimensionless using Eq. (26). The resulting dimensionless local heat transfer coefficient profile $f(x^*)$ (defined in Eq. (27) below) is plotted in Fig. 11 against the local nozzle x-coordinate. The ripples in Fig. 11 correspond to the values under the small orifices of the nozzle while the largest peaks match the paper passing below the semicircle orifices (see Fig. 1 (d)).

$$f(x^*) = \frac{\frac{1}{a}\int_0^a h(x^*, y^*)dy^*}{\bar{h}} \tag{27}$$

After converting, for each (top and bottom) nozzle, this numerical information $f(x^*)$ into the line global x-coordinate, a local Nusselt number Nu (or alternatively a local heat transfer coefficient $h(x)$) given by Eq. (28) is integrated in the energy equation (13) of the drying model:

$$Nu(x) = \frac{h(x)d_{nozzle}}{k_{air}} = f(x)Pr_{air}^{1/3}\left(4.5 + 0.21\ Re_{ij}^{4/5}\right) \tag{28}$$

where the hydraulic diameter of the nozzle section $d_{nozzle} = 0.3$ m and air conductivity k_{air} at 100 °C (equal to $0.03\frac{W}{mK}$) have been used as characteristic length and thermal conductivity. The Reynolds number of the flow inside each nozzle ij is defined by:

$$Re_{ij} = \frac{U_{ij}d_{nozzle}}{\nu_{air}} \tag{29}$$

where ν_{air} is the air kinematic viscosity also taken, for simplicity, at 100 °C of temperature and equal to $2.3\times10^{-5}\frac{m^2}{s}$. Typical Reynolds numbers in the nozzles are of the order of 10 000. The air Prandtl number Pr_{air} is taken as constant and equal to 0.7.

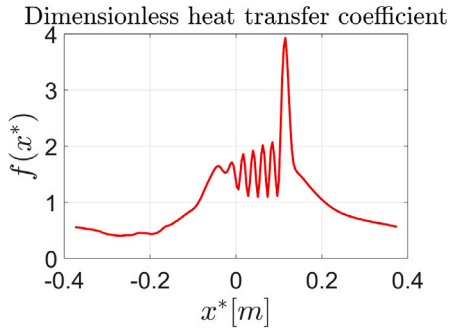

Fig. 11. Dimensionless function $f(x^*)$ for the heat transfer coefficient.

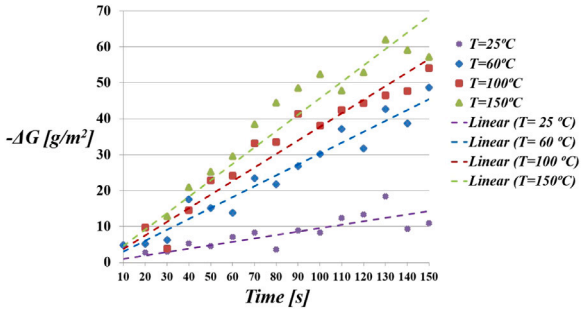

Fig. 12. Values of the experimental weight losses vs. time for each furnace temperature and the adjusted linear tendency lines.

3.3.2. Mass transfer coefficient profile $h_m(x)$

Given the complex nature of the water transport and evaporation in the resin impregnated paper, the mass transfer coefficients will depend strongly on both the intrinsic characteristics of the paper and the resin applied on it. Thus, an experimental adjustment of them should be made for each specific paper and resin. As an example, for the validation of the drying model, a specific type of paper ("Paper #1") impregnated with melamine formaldehyde resin diluted in water was analysed. A set of simple thermo-gravimetric analyses in a muffle furnace were carried out by the company staff in their installations. The muffle furnace has a fan that moves the heated air inside it at a slow velocity, below 0.1 m/s. 60 circular samples (cut all with the same size in the punch machine) were impregnated and dried at four different constant temperatures T_∞ in the muffle furnace: 25 °C, 60 °C, 100 °C and 150 °C. The initial weight after impregnation was measured, as well as the sample weights after spending different residence times inside the furnace. The different residence times were 15 for each furnace temperature: 10, 20, 30, …, 150 s. The following equation was then used to obtain the mass transfer coefficients (with the relative humidity in the laboratory equal to HR=35%):

$$\frac{dG}{dt} = -h_{m,0}(\rho_v - \rho_{v,\infty}) = -h_{m,0}\frac{P_{v,sat}(T_\infty)}{R_v T_\infty}\left(1 - \frac{HR}{100}\right) \tag{30}$$

Measuring the differences of paper weight vs. time, the experimental adjustment of the mass transfer coefficients was done for that specific paper and impregnation fluid. The experimental values and the adjusted values using a linear fitting $h_{m,0}$ for each furnace temperature are shown in Fig. 12 and summarized in Table 4.

The exponential dependency given by Eq. (31) can be used to represent the dependency of the $h_{m,0}$ on the furnace temperature T_∞:

$$h_{m,0}[\mathrm{m/s}] = 19.075\exp(-0.029T_\infty) \tag{31}$$

with T_∞ in K.

In the line, the velocities of the impingement air in the vicinity of the paper sheet are much higher (up to 4 m/s) than the velocities inside

Table 4
Fitted values of the mass transfer coefficients adjusted from the experiment.

$T_\infty[°C]$	$h_{m,0}[m/s]$
25	$3.18\ 10^{-3}$
60	$1.23\ 10^{-3}$
100	$3.15\ 10^{-4}$
150	$8.76\ 10^{-5}$

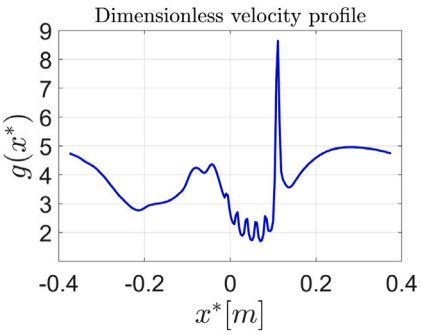

Fig. 13. Profile $g(x^*)$ for the dimensionless velocity magnitude under one nozzle, obtained from CFD simulations of two consecutive nozzles.

the muffle furnace. Therefore, the mass transfer coefficients have to be scaled to integrate the convective effect of the drying air under the furnace nozzles. To take into account that effect, information from the CFD model, previously described in Section 3.3, was used. The profile of the air velocity magnitude in the vicinity of the paper $U(x^*, y^*)$ (in a plane located at a perpendicular distance of 25 mm from the paper) was averaged in y^* direction and made dimensionless using the velocity of the air flow inside the nozzle U_{ij} (see Eq. (25)). The dimensionless velocity profile in the local nozzle coordinate $g(x^*)$ is shown in Fig. 13. Again, this profile needs to be converted into the line global x-coordinate for each (top and bottom) nozzle to obtain the global $g(x)$ distribution.

The final mass transfer coefficient $h_m(x)$, as well as the experimental mass transfer coefficient $h_{m,0}$, are made dimensionless using d_{nozzle} as characteristic length and the diffusion coefficient of water vapour in air $D_{v,air} = 2.66 \times 10^{-5} \frac{m^2}{s}$ to obtain the Sherwood number $Sh(x)$ that includes the effect of the forced convection in the paper drying:

$$Sh(x) = \frac{h_m(x) d_{nozzle}}{D_{v,air}} = C_m Sh_0(T_{\infty i}) Sc^{1/3} \left(Re_{ij}\ g(x)\right)^{4/5} \quad (32)$$

where C_m is a constant equal to 13.33 (adjusted for the studied drying line) while the Schmidt number Sc is equal to $\nu_{air}/D_{v,air}$. Therefore, the local mass transfer coefficient $h_m(x)$ from Eq. (32) is used to describe each of the (top and bottom) nozzles mass transfer coefficients in the drying model mass conservation equation (4).

4. Validation of the drying model

The drying model, defined by Eqs. (4) and (13), with the transfer coefficients given by (28) and (32), requires the following inputs, most of them related to the production conditions:

- The 110 nozzles air mass flows m_{ij}, which are given by the line air flow hydraulic model (whose inputs are described in Section 3.1.2)
- Temperatures at the two impregnation chambers (used as initial temperatures of the paper $T(0)$ and $T(x_5)$, and monitored in the line)
- Air temperature $T_{\infty i}$ inside each of the 11 furnaces (given by plenum thermocouples).
- Air specific humidity in each furnace plenum HE_i (taken from humidity sensors)
- Paper sheet velocity U_p
- Parameters related to the specific paper and resin:
  - Grammage of the non-impregnated paper G_w
  - Porosity P of the non-impregnated paper
  - Thickness of the non-impregnated paper e_w
  - Dilution of the solid resin in $Co[\%]$ of water
  - Initial grammage of the paper after impregnations, $G(0)$ and $G(x_5)$

Thus, the total number of inputs needed for the complete model prediction are up to 178. The mass transfer coefficients of Eq. (32) and constant c_ϕ are linked to a specific paper and resin used in the industrial validation of the model, so they must be re-calibrated in case of using the model for a different paper or resin. For the specific paper used in the industrial validation of the model, named "Paper #1" (of $G_w = 70\ g/m^2$), c_ϕ was equal to 2, porosity $P = 0.3$ and $e_w = 110\ \mu m$.

The model, implemented in free software GNU *Octave*, was solved employing an implicit integration scheme for the initial value problem with a discretization using 1000 divisions in the x direction for each furnace. The model predicts the paper weight $G(x)$ and temperature $T(x)$, for each combination of the production inputs, in less than 5 s.

Three complete experimental tests (Test 1, Test 2 and Test3) were carried out to validate the model with the studied paper. The validation was done by:

1. Comparing the paper temperatures (given by the line paper pyrometers) with the paper temperatures $T(x)$ provided by the numerical model.
2. Measuring experimentally the initial weights after the two impregnations (before entering furnaces 1 and 5, $G(0)$ and $G(x_5)$), which set the initial paper weight conditions, and measuring the final weights G of the paper sheet at the end of furnace 4 after the cooling section and at the end of the line, $G(x_{end\ 4})$ and $G(x_{end\ 11})$, and comparing them with the final weights predicted by the model.

The initial and final paper weights (measured and predicted by the model) for production conditions of Test 1, Test 2 and Test 3 are shown in Table 5. Figs. 14–16 show the evolution of the paper weight predicted by the model (top Figures) as well as the comparison between the predicted paper temperature and the pyrometer values (bottom figures).

The relative errors in the final paper weights are very small, with a maximum discrepancy of a 9% for Test 2. It is convenient to highlight that experimental measurements of the paper weights in the line is not an easy task to carry out. It requires to stop the production, cut (partially) the still dripping impregnated paper sheet, which is done in the paper lateral ends, put the piece of paper between plastic layers, cut the sample to a specific size and then, finally, weight the sample and subtract the plastic layer weights. The handling of the samples has to be done very carefully not to lose the impregnation fluid and that is sometimes difficult, leading, for some cases, to unrealistic values in the experimental measurements. Thus, the number of experimental validation tests with weight measurements are very limited. On the contrary, as the paper temperature is monitored continuously, indirect validation of the model through the temperature prediction can always be done. Averaged relative error for the predicted paper temperature is 7.3% for Test 1, 6.6% for Test 2 and 8.1% for Test 3. It is worth to note that the model captures very well the evolution of the paper temperature (see bottom figures of 14, 15 and 16), especially in the first part of the line. As an example, during the production of Test 3, an unexpected event took place in the heating exchanger of furnace 3 (leading to its disconnection) and the temperature of the air inside this furnace remained close to the ambient temperature. However, the model was able to mimic the final drying, showing its capability of making accurate predictions even for out of control production parameters.

Table 5
Experimental paper weight values and its comparison to the predicted values given by the model.

$G[g/m^2]$	$G(0)$	$G(x_{end\ 4})$	$G(x_{end\ 4})$ Model	$\varepsilon_1(\%)$	$G(x_5)$	$G(x_{end\ 11})$	$G(x_{end\ 11})$ Model	$\varepsilon_2(\%)$
Test 1	173	152	151.9	0.07	266	198	198.2	0.1
Test 2	207	158	172.4	9	257	196	197.7	0.9
Test 3	178	150	148.8	0.13	262	198	198.8	0.1

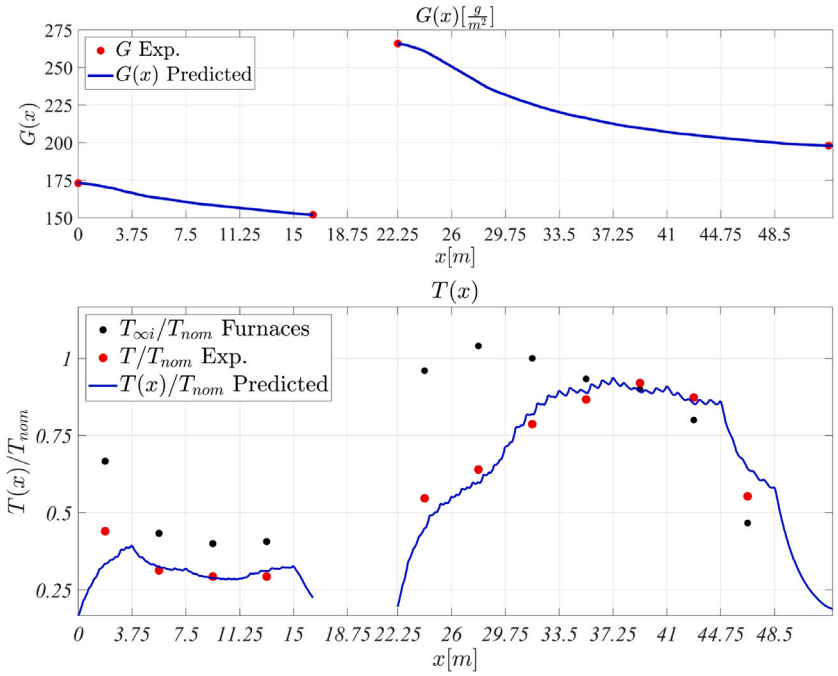

Fig. 14. Comparison between predicted and experimental values for the paper weight and paper temperature values for Test 1 production conditions.

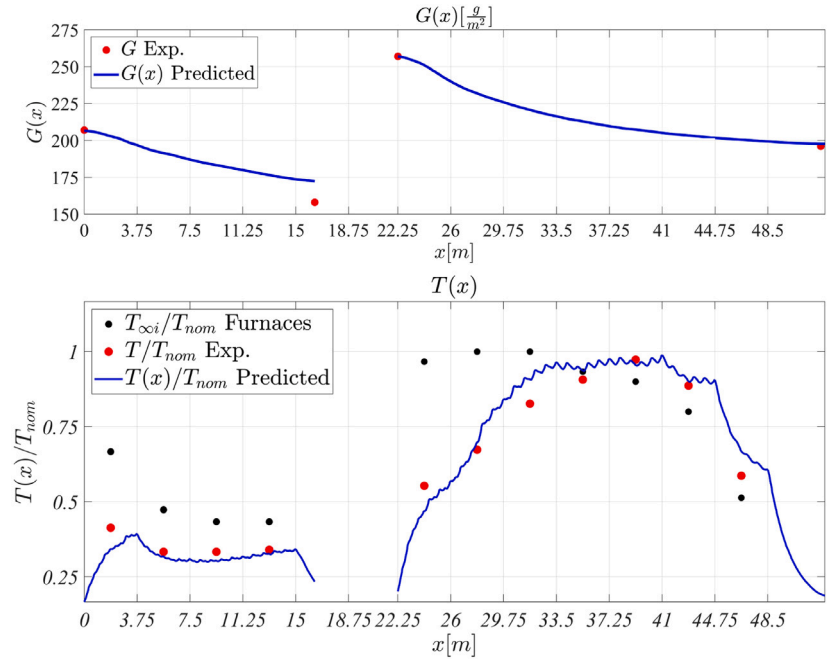

Fig. 15. Counterpart of Fig. 14 for Test 2 production conditions.

5. Some applications of the developed model

The model developed and validated in the previous sections can be very relevant for a (large) number of engineering applications. According to the methodology proposed in this paper, drying process modelling involves two different phases: (a) A first off-line phase, corresponding to the model preparation. Based on a detailed modelling of air flows near the paper along the whole line (which involves 3D CFD simulations), the model provides an accurate prediction of paper drying, as showed in the validation carried out above. This phase

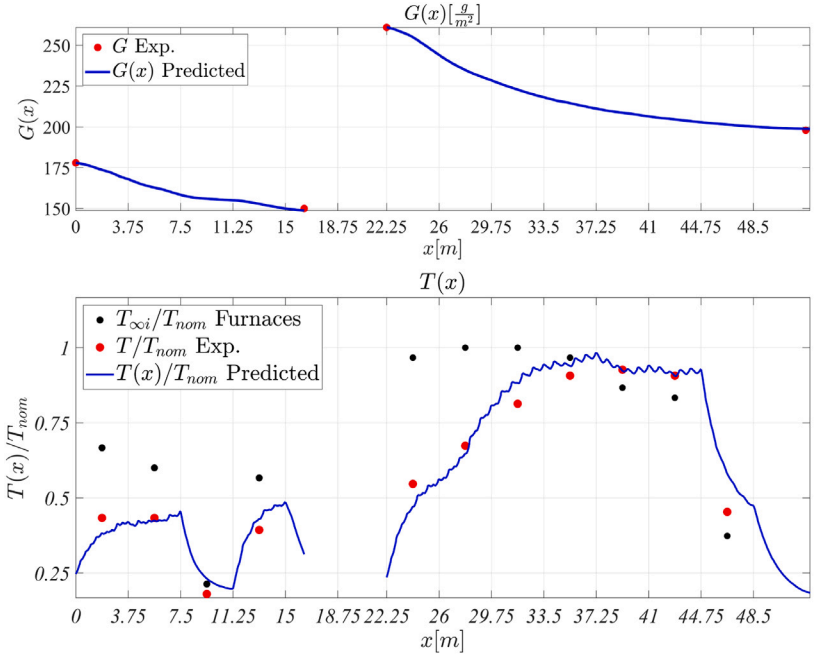

Fig. 16. Counterpart of Fig. 14 for Test 3 production conditions.

is indeed expensive in both computational and experimental terms. And (b), a final on-line phase, corresponding to the drying prediction for a particular combination of operation parameters (which is very inexpensive) using the model prepared in the previous phase. Once all the details have been incorporated into the model, the prediction tool is very fast (in this paper, a model development implementation using GNU/Octave is presented, but translating the model programming to C++ or Fortran can provide a speed-up factor of 100 or larger in the execution time and would be easily linked to a Python, GNU/Octave or MATLAB script). In this section, several applications of the fast and accurate tool resulting from the second, on-line phase are considered.

Availability of an accurate and fast model of the whole drying line (that use line operation parameters as inputs) provides a very valuable tool to deal with engineering tasks such as: sensitivity analysis of the line operation conditions, optimization of the line operation conditions (see examples [43,44] for other industrial processes), line adaption to a new product, or the implementation of an efficient line automatic control based on model predictive control techniques. In any of these applications, both accuracy and a low computational cost are essential.

In this section, two examples are provided: first, a sensitivity analysis of the model, and second, an example of optimization of the line operation conditions

5.1. Sensitivity analysis of the model

An example of a sensitivity analysis of the model outcomes to the production conditions was carried out using the Test 1 conditions as base for the variations. Fig. 17 shows the paper weight evolution for different variations of the production conditions U_p, θ_{ij}, rpm_i, $T_{\infty,i}$:

- Fig. 17(a) shows that deviations of ±30% in the paper velocity U_p lead to deviations in the final paper weight of ±3.3%.
- Fig. 17(b) displays the paper weight evolution when the nozzle gates of furnaces 6, 7 and 8 are practically closed. The paper final weight deviations are of a 2.1% for this example.
- Fig. 17(c) highlights the effect of setting the furnaces fan velocities in furnaces 5 to 11 to 53%$rpms_{nom}$ (from the corresponding values of $rpm/rpm_{nom}[\%]$ =[57, 57, 57, 53, 53, 47, 47] for Test1). An average change of a 7.8% in the $rpms$ values, leads to differences in the final paper weight of a 2.6%.
- Finally, Fig. 17(d) reflects the effect of limiting the furnace temperature T_∞ of furnaces 5 to 11 from $T_\infty/T_{nom}[\%]$ =[97, 100, 100, 93, 90, 80, 51] to 67%. The relative variation in the final paper weight for this example was 1.3%.

Of course, predictions of any combined deviation of production parameters can also be obtained. It is convenient to notice that the admissible deviations in the final paper weight during production are ±5 g/m^2, which generally represents a weight percentage of approximately 2.5%. Therefore, the sensitivity of the model outcomes is of the same order. The sensitivity results suggest that, apart from the paper velocity, the most efficient mechanism to control the drying process is the rpm adjustment of the furnaces fans, especially if a quick response is wanted, as the model depends more weakly on the furnaces temperatures and the temperature variations (particularly decreasing furnace temperatures) takes a longer time to adjust due to the specific design of the installation.

5.2. Optimization of the drying process parameters

The model, coupled to an optimization algorithm, can be used as a tool for the inverse design of the production conditions. The purpose is to find out, with a reduced computational time, the best operational parameters of the process according to a specific criterion, as for example, the minimization of a certain functional $f(\vec{z})$. The minimization problem was solved using the drying model combined with a constrained nonlinear optimization using a sequential quadratic programming (SQP) algorithm [45] implemented in GNU/Octave ‘‘nonlin_min’’ package and available under the ‘‘fmincon’’ function (an interface to ‘‘nonlin_min’’ implemented for compatibility with MATLAB optimization functions). In the quadratic model (of the objective function) first order derivatives in the function gradient are computed using finite differences and Hessian matrix is approximated using a Broyden BFGS technique.

As an example of the functionalities of the model, the objective function (33), which evaluates the deviation from a reference weight curve (discretized in 11 points along the line, one per furnace) was minimized:

$$\min_{\vec{z}} \quad \sum_{i=1}^{11} \left(\frac{|G(x_i,\vec{z}) - G(x_i)^{ref}|}{G(x_i)^{ref}} \right)^2 \tag{33}$$

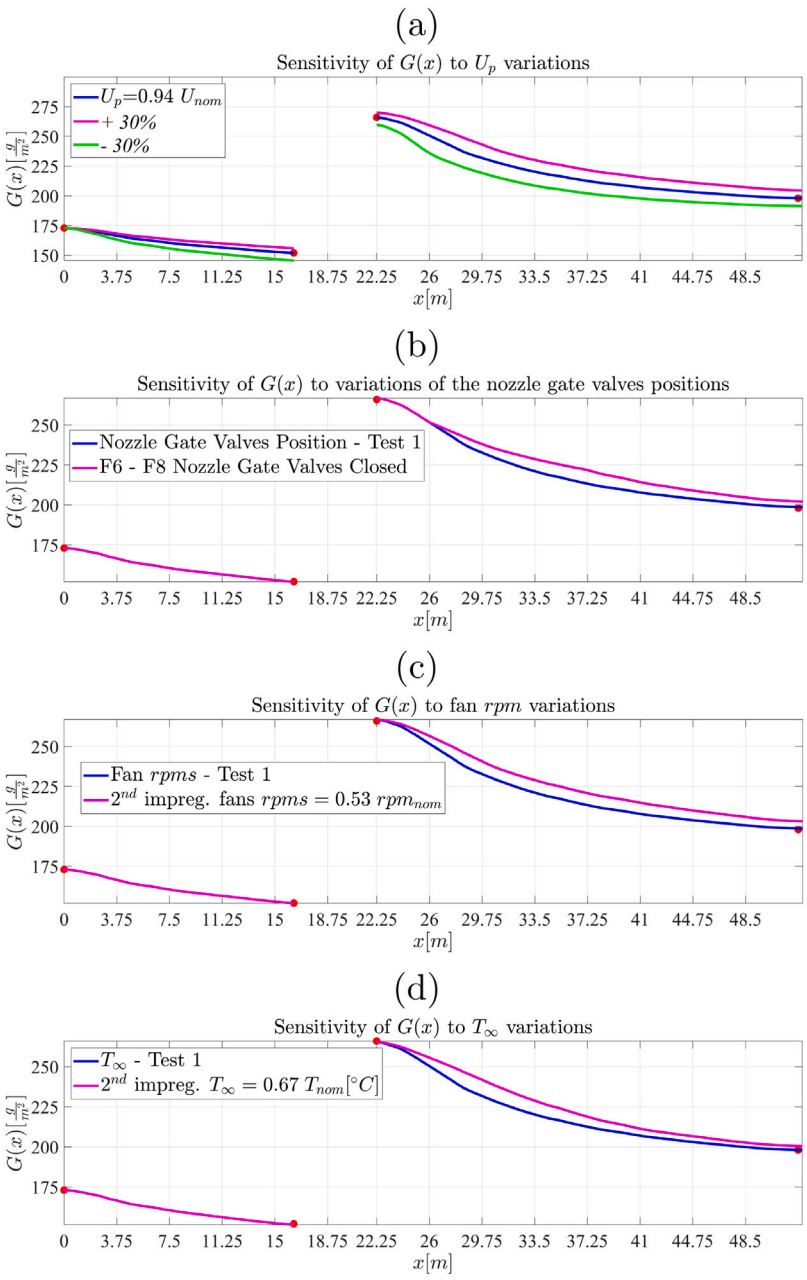

Fig. 17. Sensitivity of paper weight evolution for variations of Test 1 production conditions.

where the searched production parameter vector $\vec{z}$ (that minimized the functional) was a 11 element vector which contains each relative furnace fan rpms $r_i[\%] = \frac{rpm_i}{rpm_{nom}}$:

$$\vec{z} = (r_1, r_2, r_3, r_4, r_5, r_6, r_7, r_8, r_9, r_{10}, r_{11}) \tag{34}$$

The problem defined in (33) was solved with the following restrictions over vector $\vec{z}$:

$$13\% \leq r_i \leq 100\% \tag{35}$$

The reference paper weight values are shown in Fig. 18 (see pink crosses). The optimization tool run coupled to the model provided the following selection of production parameters (relative fans rpms) for the given reference curve:

$$\vec{z} = (33.3\%, 33.3\%, 33.7\%, 70.9\%, 100\%, 75.8\%, 86.9\%, 39.9\%, 28.1\%, 30.4\%)$$

Differences between the prescribed paper weights (used as reference values) and the predicted paper weight values with the optimized production inputs are below 0.23% (averaged relative differences).

6. Conclusions

A new methodology to build an accurate model for the prediction of the drying of impregnated paper in a continuous furnace line has been presented. First, an accurate prediction of the local drying conditions resulting from the line operation parameters is required. Although a large computational cost is needed during the model preparation (involving some detailed three-dimensional computational fluid dynamic computations), this detailed information is then incorporated, in the proposed methodology, into a hydraulic model able to predict (with a very low computation cost) the local drying conditions as a function of the line operation parameters.

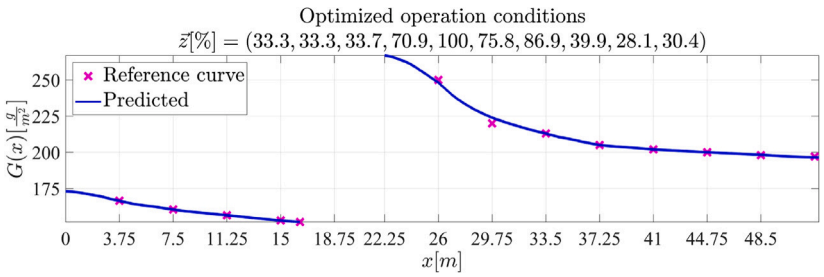

Fig. 18. Optimized production parameters for a given paper weight curve (pink).

Using those local drying conditions, a detailed model for the paper drying is then formulated. Likewise, this drying model incorporates information from the experimental paper drying kinetics (under controlled conditions in a muffle furnace), as well as from a reduced number (three) of detailed three-dimensional thermal-fluid computations around the paper sheet. The resulting (fast) predictive model has been validated with the real production data, showing its ability to provide accurate predictions for the evolution of the paper drying, retaining local details of the process.

The drying model needs a characterization of the initial paper impregnation, since these are the initial conditions for the drying process considered in this paper. In the experiments described in this paper, impregnation is estimated by a complicated manual process described in Section 3. To overcome this drawback and extend the usefulness of the model, this characterization can be replaced by an on-line estimation using near infrared spectroscopy measurements as described, for instance, in [33].

A great advantage of this model is its straightforward adaptation to a different resin impregnated paper or industrial drying line:

- One key model ingredient concerns evaporation kinetics and transport (through paper pores) properties for resin solutions, since available data in the literature are very scarce. It should be noted that capillary effects are very relevant in both mechanisms and strongly dependent on the solution composition. As a result, model adaptation to a different resin (or a different paper) requires the characterization of the new product drying by realization of simple drying measurements under controlled conditions (e.g in a muffle furnace).
- The spatial drying pattern created on the paper surface is associated to the geometrical arrangement of the nozzles orifices. This information is embedded in the model through results from three 3D-thermal-fluid computations around the paper sheet, which can be carried out (if needed) for different nozzle configurations.

Additionally, as the thermal-fluid simulations of the paper drying retains the two-dimensional drying pattern along the paper surface (see example in Fig. 10), the model, after some future adaptations (e.g., two-dimensional drying model coupled with a mechanical modelling of the paper), come in useful to study the effects of the uneven drying patterns on the paper shrinkage, in order to improve the quality of the final product in the industrial air impingement drying line.

The derivation of a fast and accurate drying model, as done in this paper, offers a clear possibility for solving very efficiently a large number of engineering tasks related to the considered industrial drying process (including line operation optimization, inverse design or line automatic control) in the framework of the increasingly relevant role of mathematical models (digital twins in Industry 4.0 jargon) in industrial applications.

Declaration of competing interest

The authors declare that they have no known competing financial interests or personal relationships that could have appeared to influence the work reported in this paper.

Acknowledgements

This research was supported by the spanish Instituto Tecnológico de Matemática Industrial (ITMATI) [Grant Numbers: C69-2019, C80-2020, C83-2020].

Funding for open access charge: Universidade de Vigo/CISUG.

Appendix A. Supplementary data

Supplementary material related to this article can be found online at https://doi.org/10.1016/j.applthermaleng.2021.117602.

References

[1] A.S. Mujumdar, Handbook of Industrial Drying, fourth ed., CRC Press, 2014.
[2] J.R. Philip, Annual review of fluid mechanics, Annu. Rev. Fluid Mech. 2 (1970) 177–204.
[3] C.Y. Wang, P. Cheng, Multiphase flow and heat transfer in porous media, Adv. Heat Transf. 30 (1997) 93–196.
[4] S. Beyhaghia, K.M. Pillaia, D.T. Qadahb, M.L. Dietz, Evaporation and transport of non-dilute, multi-component liquid mixtures inporous wicks: Simulation and experimental validation, Int. J. Heat Mass Transfer 54 (2011) 5216–5230.
[5] M.J. Varady, T.P. Pearl, S.A. Bringuier, B.A. Mantooth, Vapor emission from porous materials with diffusive transport in the solid–phase, Int. J. Heat Mass Transfer 114 (2017) 758–768.
[6] I.N. Tsimpanogiannis, Y.C. Yortsos, S. Poulou, N. Kanellopoulos, A.K. Stubos, Scaling theory of drying in porous media, Phys. Rev. E 59 (4) (1999) 4353–4365.
[7] M. Prat, Recent advances in pore-scale models for drying of porous media, Chem. Eng. J. 86 (2002) 153–164.
[8] A.G. Yiotis, A.K. Stubos, A.G. Boudouvis, I.N. Tsimpanogiannis, Y.C. Yortsos, Pore-network modeling of isothermal drying in porous media, Transp. Porous Med. 58 (2005) 63–86.
[9] M. Prat, On the influence of pore shape, contact angle and film flows on drying of capillary porous media, Int. J. Heat Mass Transfer 50 (2007) 1455–1468.
[10] E. Shahraeeni, D. Or, Pore-scale analysis of evaporation and condensation dynamics in porous media, Langmuir 26 (17) (2010) 13924–13936.
[11] A.A. Moghaddam, A. Kharaghani, E. Tsotsas, M. Prat, A pore network study of evaporation from the surface of a drying non–hygroscopic porous medium, AIChE J. 64 (4) (2018) 1435–1447.
[12] T. Defraeye, B. Blocken, D. Derome, B. Nicolai, J. Carmeliet, Convective heat and mass transfer modelling at air–porous material interfaces: Overview of existing methods and relevance, Chem. Eng. Sci. 74 (2012) 49–58.
[13] T. Defraeye, Advanced computational modelling for drying processes, Rev. Appl. Energy 131 (2014) 323–344.
[14] A. Halder, A.K. Datta, Surface heat and mass transfer coefficients for multiphase porous media transport models with rapid evaporation, Food Bioprod. Process. 90 (2012) 475–490.
[15] T. Defraeye, B. Blocken, J. Carmeliet, Influence of uncertainty in heat–moisture transport properties on convective drying of porous materials by numerical modelling, Chem. Eng. Res. Des. 91 (2013) 36–42.
[16] W. Masmoudi, M. Prat, Heat and mass transfer between a porous medium and a parallel external flow. application to drying of capillary porous materials, Int. J. Heat Mass Transfer 34 (8) (1991) 1975–1989.
[17] T. Lu, P. Jiang, S. Shen, Numerical and experimental investigation of convective drying in unsaturated porous media with bound water, Heat Mass Transfer 41 (2005) 1103–1111.
[18] F.A. Khan, A.G. Straatman, A conjugate fluid-porous approach to convective heat and mass transfer with application to produce drying, J. Food Eng. 179 (2016) 55–67.
[19] M. Ilic, I.W. Turner, Convective drying of a consolidated slab of wet porous material, Int. J. Heat Mass Transfer 32 (12) (1989) 2351–2362.

[20] Y. Tang, J. Min, Water film coverage model and its application to the convective air-drying simulation of a wet porous medium, Int. J. Heat Mass Transfer 131 (2019) 999–1008.
[21] V.V. Rao, O. Trass, Mass transfer from a flat surface to an impinging turbulent jet, Can. J. Chem. Eng. 42 (3) (1964) 95–99.
[22] J.H. Masliyah, T.T. Nguyen, Mass transfer due to an impinging slot jet, Int. J. Heat Mass Transfer 22 (1979) 237–244.
[23] Q. Chen, V. Modi, Mass transfer in turbulent impinging slot jets, Int. J. Heat Mass Transfer 42 (1999) 873–887.
[24] A.L. Ljung, L.R. Andersson, A.G. Andersson, T.S. Lundström, M. Eriksson, Modelling the evaporationrrate in an impingement jet dryer with multiple nozzles, Int. J. Chem. Eng. (2017) 5784627.
[25] I.H. Khan, Z. Welsh, Y. Gu, M.A. Karim, B. Bhandari, Modelling of simultaneous heat and mass transfer considering the spatial distribution of air velocity during intermittent microwave convective drying, Int. J. Heat Mass Transfer 153 (2020) 119668.
[26] J.F. Bond, Drying paper by impinging jets of superheated steam: Drying rates and thermodynamic cycles (Ph.D. dissertation), McGill University, 1991.
[27] A.B. Etemoglu, M. Can, A. Avci, E. Pulat, Theoretical study of combined heat and mass transfer process during paper drying, Heat Mass Transfer 41 (2005) 419–427.
[28] S.J. Hashemi, S. Sidwall, W.J. Murray Douglas, Paper drying: a strategy for higher machine speed. ii. impingement air drying for hybrid dryer sections, Drying Technology 19 (10) (2001) 2509–2530.
[29] S. Stenström, Drying of paper: A review 2000–2018, Drying Technol. 38 (7) (2020) 825–845.
[30] S.J. Hashemi, W.J. Murray Douglas, Paper drying: A strategy for higher machine speed. I. through air drying for hybrid dryer sections, Drying Technology 19 (10) (2001) 2487–2507.
[31] L. Nilson, Heat and mass transfer in multicylinder drying. Part I. Analysis of machine data, Chem. Eng. Process. 43 (2004) 1547–1553.
[32] M. Kohlmayr, J. Stultschnik, A. Teischinger, A. Kandelbauer, Drying and curing behaviour of melamine formaldehyde resin impregnated papers, J. Appl. Polym. Sci. 131 (2014) 1–9 39860.
[33] M. Gonçalves, M. Ribeiro, N.T. Paiva, J.M. Ferra, J. Martins, F. Magalhães, L. Carvalho, Resin and volatile content of melamine-impregnated paper assessed by near infrared spectroscopy, a simulation of the industrial process using a laboratory-scale gantry, Eur. J.f Wood Wood Products 78 (2020) 1279–1286.
[34] L. Sivill, P. Ahtila, M. Taimisto, Thermodynamic simulation of dryer section heat recovery in paper machines, Appl. Therm. Eng. 25 (2005) 1273–1292.
[35] L. Kong, Z. Tao, H. Liu, D. Zhang, Effect of operating parameters on the drying performance of multicylinder paper machine dryer section, Drying Technol. 34 (13) (2016) 1641–1650.
[36] O. Slatteke, Modeling and Control of the Paper Machine Drying Section (Ph.D. dissertation), Lund University, 2006.
[37] M.G.A. Vieira, L. Estrella, S.C.S. Rocha, Energy efficiency and drying kinetics of recycled paper pulp, Drying Technol. 25 (10) (2007) 1639–1648.
[38] L. Sivill, P. Ahtila, Energy efficiency improvement of dryer section heat recovery systems inpaper machines – a case study, Appl. Therm. Eng. 29 (17–18) (2009) 3663–3668.
[39] S. Ghodbanan, R. Alizadeh, S. Shafiei, Optimization for energy consumption in drying section of fluting paper machine, Thermal Sci. 21 (3) (2017) 1419–1429.
[40] F.M. White, Fluid Mechanics, McGraw Hill, 2011.
[41] F.P. Incropera, D.P. DeWitt, Introduction To Heat Transfer, John Wiley Sons, 2002.
[42] J. Blazek, Computational Fluid Dynamics - Principles and Applications, third ed., Elsevier, 2015.
[43] E. Martín, M. Meis, C. Mourenza, D. Rivas, F. Varas, Fast solution of direct and inverse design problems concerning furnace operation conditions in steel industry, Appl. Therm. Eng. 47 (2012) 41–53.
[44] E. Martín, F. Varas, I. Viéitez, Reduced-order modeling in the manufacturing process of wire rod: Applications for fast temperature predictions and optimal selection of process parameters, Adv. Link. Math. Ind., SxI - Springer Innov., Springer Int. Publishing 15 (2021) (2021) 59–74.
[45] J. Nocedal, S.J. Wright, Numerical Optimization, second ed., Springer Science Business Media, 2006.